

An X-ray chimney extending hundreds of parsecs above and below the Galactic Centre

G. Ponti^{1,2*}, F. Hofmann¹, E. Churazov^{3,4}, M. R. Morris⁵, F. Haber¹, K. Nandra¹, R. Terrier⁶, M. Clavel⁷ & A. Goldwurm^{6,8}

Evidence has mounted in recent decades that outflows of matter and energy from the central few parsecs of our Galaxy have shaped the observed structure of the Milky Way on a variety of larger scales¹. On scales of 15 parsecs, the Galactic Centre has bipolar lobes that can be seen in both the X-ray and radio parts of the spectrum^{2,3}, indicating broadly collimated outflows from the centre, directed perpendicular to the Galactic plane. On larger scales, approaching the size of the Galaxy itself, γ -ray observations have revealed the so-called ‘Fermi bubble’ features⁴, implying that our Galactic Centre has had a period of active energy release leading to the production of relativistic particles that now populate huge cavities on both sides of the Galactic plane. The X-ray maps from the ROSAT all-sky survey show that the edges of these cavities close to the Galactic plane are bright in X-rays^{4–6}. At intermediate scales (about 150 parsecs), radio astronomers have observed the Galactic Centre lobe, an apparent bubble of emission seen only at positive Galactic latitudes^{7,8}, but again indicative of energy injection from near the Galactic Centre. Here we report prominent X-ray structures on these intermediate scales (hundreds of parsecs) above and below the plane, which appear to connect the Galactic Centre region to the Fermi bubbles. We propose that these structures, which we term the Galactic Centre ‘chimneys’, constitute exhaust channels through which energy and mass, injected by a quasi-continuous train of episodic events at the Galactic Centre, are transported from the central few parsecs to the base of the Fermi bubbles⁴.

Figure 1 shows an X-ray image of the central 300×500 parsecs or so of the Milky Way, which we obtained via observations with the XMM-Newton satellite between 2016 and 2018, in addition to archival data⁹. Strong, low-energy photo-absorption that hinders the mapping of the large-scale diffuse emission in the Galactic Centre region with ROSAT is alleviated in this image by using the wider energy band of XMM-Newton (see Methods). The Galactic supermassive black hole, manifested as the radio source Sagittarius A* (Sgr A*), and its surrounding central cluster of massive stars¹⁰ are located at the centre, as are the ± 15 -pc bipolar lobes, visible in Fig. 1 as a barely resolved small white region perpendicular to the plane. Two new features appear in this image as elongated and slightly edge-brightened structures (at least 1° or 160 pc across) to the north and south of Sgr A*. We refer to these quasi-linear features as the northern and southern Galactic Centre chimneys. The northern chimney is roughly co-spatial with the Galactic Centre lobe. Both chimneys have comparable X-ray brightness and colour. This suggests that they have a common origin that is probably connected with the Galactic Centre, and a common emission mechanism. Despite their similarities, the northern and southern chimneys are not strictly symmetric about the Galactic plane, which can plausibly be attributed to ‘Galactic weather’, that is, the differences in the relatively dense interstellar medium structures above and below the plane that interact or interfere with the Galactic Centre outflows of mass and energy that have presumably formed the chimneys.

Along the Galactic plane, the breadth of the newly discovered features is limited to ± 50 pc ($\pm 0.4^\circ$), while in the latitudinal direction,

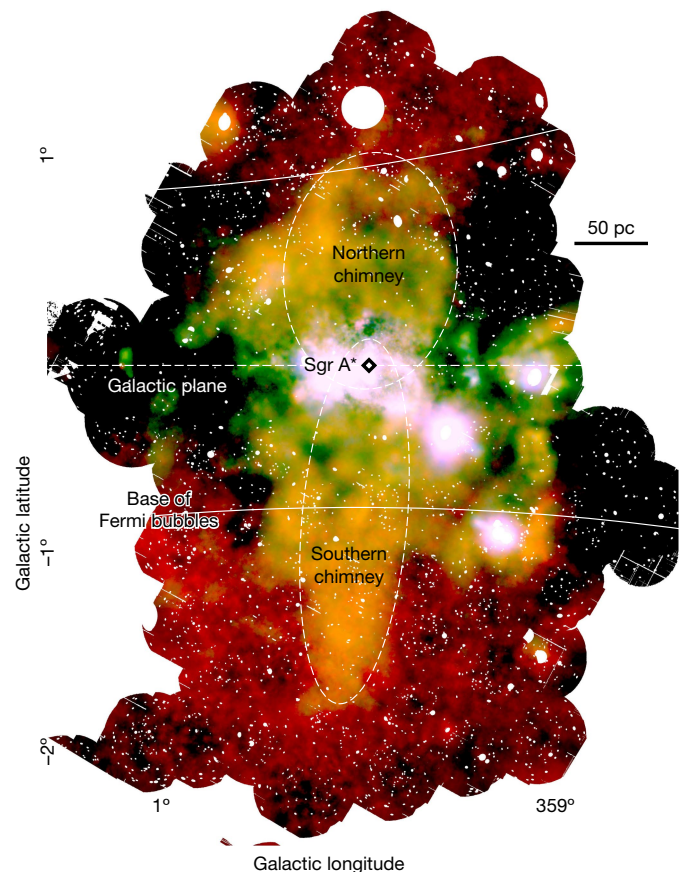


Fig. 1 | X-ray emission from the central 300 pc by 500 pc of the Milky Way. The red–green–blue (RGB) image shows integrated emission in the energy range 1.5–2.6 keV (red); integrated emission from 2.35 keV to 2.56 keV, corresponding to the S xv transition (green); and continuum emission in the 2.7–2.97-keV band, which is therefore not contaminated by the intense S xv and Ar xvii lines (blue)⁹. Sgr A*, the electromagnetic counterpart of the supermassive black hole, and the central cluster of massive stars, are located at the centre. A coherent edge-brightened shell-like feature with a diameter of about 160 pc, dubbed the northern ‘chimney’, is present north of Sgr A*. The shell is roughly co-spatial with the radio feature known as the Galactic Centre lobe⁸. Diametrically opposite to the chimney with respect to Sgr A* is the bright and elongated feature dubbed the southern chimney. The north and south features have comparable brightness, extent and colour, suggesting a similar emission process (see regions enclosed by white dashed lines). Their relative placement suggests a common origin located close to Sgr A*. The white arcs correspond to the low-latitude edges of the Fermi bubbles, as extrapolated by ROSAT X-ray emission at higher latitudes (see Extended Data Fig. 1). Point sources have been removed. Larger white areas correspond to regions that have been excised to remove the dust-scattering haloes around bright sources.

¹Max-Planck-Institut für Extraterrestrische Physik, Garching, Germany. ²INAF-Osservatorio Astronomico di Brera, Merate, Italy. ³Max-Planck-Institut für Astrophysik, Garching, Germany. ⁴Space Research Institute (IKI), Moscow, Russia. ⁵Department of Physics and Astronomy, University of California, Los Angeles, CA, USA. ⁶Unité mixte de recherche Astroparticule et Cosmologie, Paris, France. ⁷Université Grenoble Alpes, CNRS, IPAG, Grenoble, France. ⁸Département d’Astrophysique (DAP), IRFU/DRF/CEA-Saclay, Gif-sur-Yvette, France. *e-mail: gabriele.ponti@inaf.it

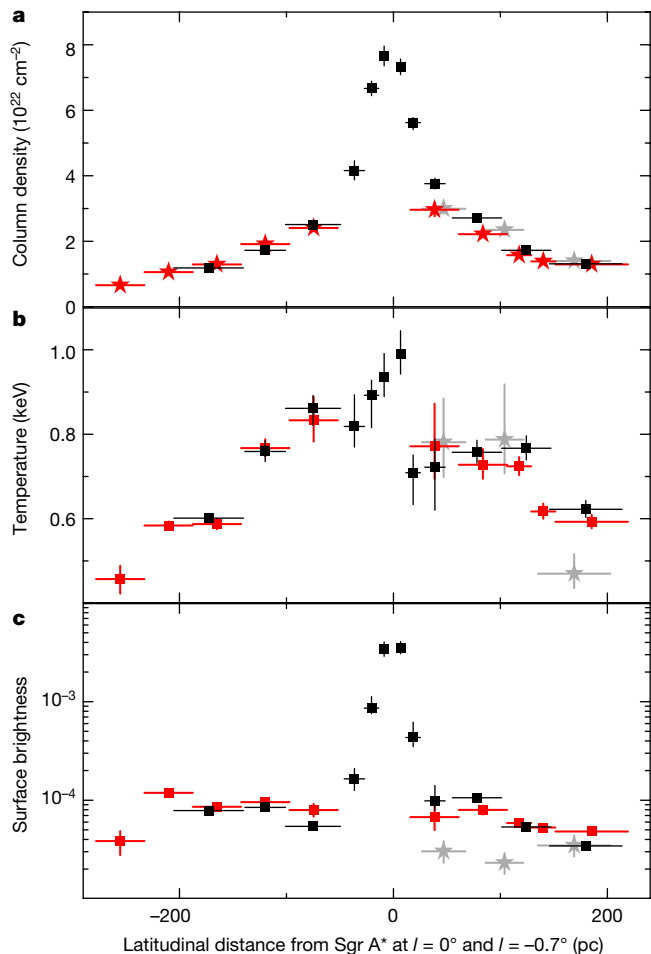


Fig. 2 | Latitudinal variation of the physical parameters of the Galactic Centre X-ray plasma. Positive values indicate Galactic north. The latitude is given in parsecs, assuming that the emission is located at the Milky Way centre. **a–c**, Latitudinal profiles of the column density of neutral absorbing material (**a**), temperature (**b**) and surface brightness (**c**) (see Methods) of the X-ray-emitting thermal plasma at $l = 0^\circ$ are shown, as derived from the fit of the Chandra (black squares) and XMM-Newton (red squares) spectra (see Extended Data Fig. 5). Grey stars show the latitudinal profile at $l = -0.7^\circ$ as derived from the fit to XMM-Newton spectra (see Methods). Vertical error bars represent 1σ uncertainties; horizontal error bars show the radial range of the extraction regions.

the chimneys span more than a degree above and below the plane, where they merge with much more extended warm plasma emission seen by ROSAT and tentatively identified as the X-ray counterparts of the Fermi bubbles^{4,5,11} (see Methods; Extended Data Fig. 1). Towards the plane, the chimneys can be traced down to $b \approx \pm 0.2^\circ$. Morphologically, they appear to originate from a region within about 50 pc of Sgr A*, with the ± 15 -pc bipolar lobes nested at the centre.

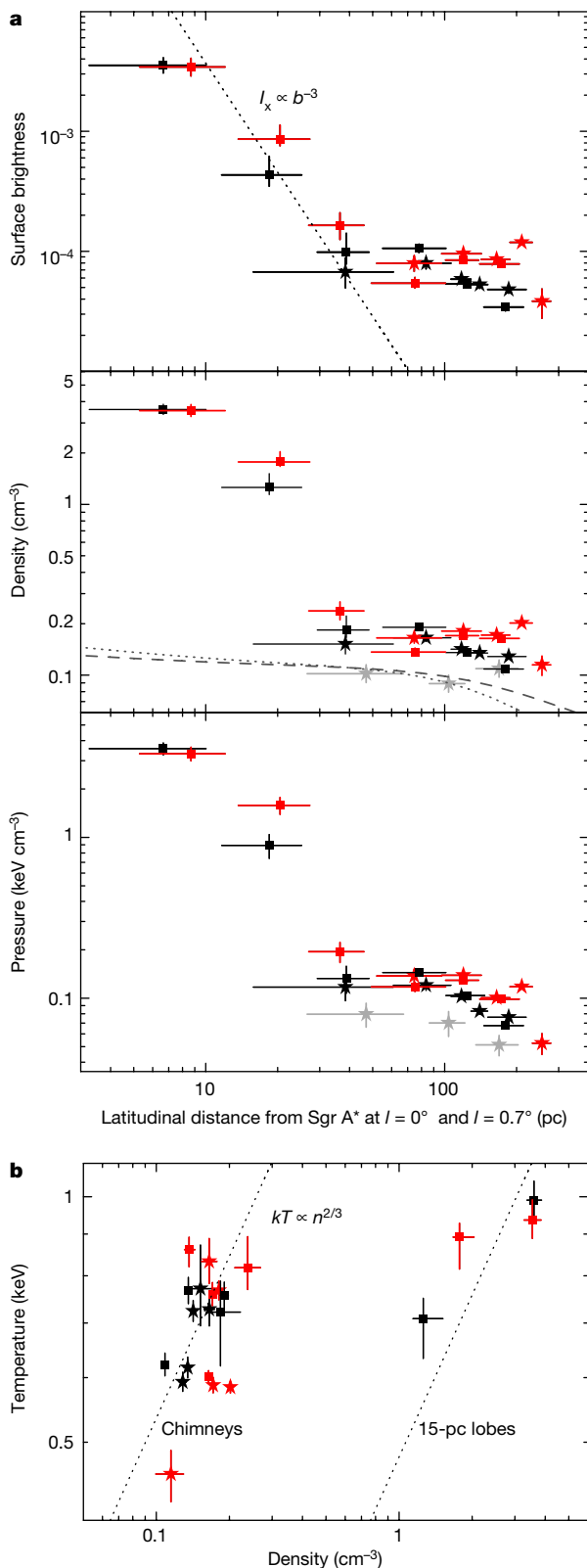
These ± 15 -pc bipolar lobes are traced down to the parsec scale by plasma with temperature $kT \approx 0.7$ –1 keV. Their X-ray surface brightness declines rapidly with latitude $I_x \propto b^{-2}$ to b^{-3} between a few to about 15 pc (refs^{8,11,12}), indicating a strong pressure gradient (see Figs. 2, 3). Such a pressure gradient cannot be compensated by the gravitational potential of the central region, so the gas in the bipolar lobes must be outflowing (Fig. 3). Under the assumption of freely expanding conical or paraboloidal outflow¹³, the temperature should drop rapidly with latitude owing to adiabatic expansion, converting it into a fast and cold gas stream. Such a situation is often invoked for the extra-planar outflows in star-forming galaxies^{14–16}, where the observed X-rays are merely tracers of a much more powerful energy- and mass-loaded outflow.

Alternatively, the observed X-rays could be coming from the shock-heated gas that surrounds the lobes, reminiscent of active galactic nuclei (AGN)-inflated bubbles in galaxy clusters. In this framework, the temperature of the gas should characterize the expansion velocity of the lobes. Observations with X-ray calorimeters and X-ray coverage of the full extent of the base of the Fermi bubbles are needed to clarify this. Indeed, if the Fermi features are the equivalent of AGN-inflated structures, then the chimneys should be unique in the Milky Way.

To obtain a conservative lower limit on the power of the ± 15 -pc structure, we assume that the X-ray gas is volume-filling and that the outflow velocity is comparable to the speed of sound, $c_s \approx 500 \text{ km s}^{-1}$, set by the gas temperature. The thermal energy of the ± 15 -pc lobes is then approximately $6 \times 10^{50} \text{ erg}$ and the power of the outflow averaged over the sound-crossing time of the lobes, $t_s \approx 3 \times 10^4 \text{ yr}$, is $L_{15 \text{ pc}} \approx 8 \times 10^{38} \text{ erg s}^{-1}$. These are relatively modest requirements in terms of the time-averaged energetics that could be satisfied by accretion-powered events from the Galactic Centre black hole, which may arise, for example, from tidal disruption of stars, releasing 10^{51} erg to 10^{52} erg every few thousand years^{17,18} and by supernovae explosions in the central star cluster¹⁹. If the X-ray-emitting gas has a very low filling factor, then the actual energetics of the ± 15 -pc outflow could be much larger than the values quoted above.

At latitudes larger than $\pm 15 \text{ pc}$, the X-ray emission from the ± 15 -pc bipolar lobes blends into the more extended emission of the chimneys. Within the northern chimney, the plasma temperature remains roughly constant at $kT \approx 0.7$ –0.8 keV over its entire extent (about 160 pc; Fig. 2). This and the shell-like morphology of the northern chimney are easily understood if this mild outflow encounters a cap partly obstructing its further latitudinal expansion⁸. The density within the chimneys gently decreases with latitude from about 0.2 cm^{-3} at 30 pc to about 0.1 cm^{-3} at 160 pc. The thermal energy in the chimneys, derived from the X-ray data as is done above for the ± 15 -pc lobes, is about $4 \times 10^{52} \text{ erg}$. Using again the sound-crossing time of the 160-pc structure ($t_s \approx 3 \times 10^5 \text{ yr}$) as an estimate for the energy replenishment time, we obtain the power $L_{160 \text{ pc}} \approx 4 \times 10^{39} \text{ erg s}^{-1}$. Although this is a factor of 5 higher than the estimated power for the ± 15 -pc lobes, it is still consistent with being driven by supernovae or tidal disruption events. We note that for the plasma in the chimneys, the effect of the Galactic gravitational potential gradient may not be negligible; therefore the $kT \approx 0.7 \text{ keV}$ plasma might be close to hydrostatic equilibrium (Fig. 2), rather than outflowing at the sound speed. In this context, the chimneys could represent the channel excavated by powerful outflows associated with a series of past episodic events and connecting the Galactic Centre with the halo. They might have transported substantially more energy (for example, AGN-like activity) than the residual thermal energy currently radiated. The long cooling time (about $2 \times 10^7 \text{ yr}$) and the shallow density gradient in the vertical direction do not contradict this framework. At the same time, the edge-brightened morphology of the chimneys is also consistent with an ongoing dark (for example, cold or low-density) flow setting, when X-rays at the edges are due to the flow interaction with the denser interstellar medium.

The chimneys appear to be well confined in the longitudinal direction, except for a ‘protrusion’ on the eastern side of the northern chimney (see Methods), and they have sharp edges along much of their vertical extent (Extended Data Figs. 1–3). Given the estimated pressure of the X-ray-emitting gas in the chimneys ($P \approx 0.1$ –0.2 keV cm^{-3}), it seems plausible that either dense interstellar medium phases or magnetic pressure ($p \approx B^2/8\pi$ corresponding to $B \gtrsim 60$ –90 μG would be required) can provide the necessary confinement. For example, radio surveys of the central few degrees indicate a rather strong magnetic field^{20–22}, rising vertically from the central molecular zone. The roughly cylindrical shape of the chimneys and their widths of about 100 pc at $b > \pm 0.2^\circ$ raise the possibility that they are formed by a distributed energy injection process in the plane, evidence that would favour a star-formation-powered mechanism. This is corroborated by the observations that the majority of the evolved massive stars of the central molecular zone are concentrated near the base of the chimneys^{23,24}.



It is worth noting that for a flow through a cylindrical channel having a constant cross-section, the pressure experiences a modest drop (by a factor of about 2) owing to the adiabatic acceleration of the gas along the channel and the work done against the Galactic gravitational potential, but can drop dramatically once the channel widens. The observed temperature of the gas in the chimneys, if viewed as a proxy for a typical energy-per-particle value for injected energy and mass, also appears to be within a factor of a few of what is usually assumed in star-formation-driven frameworks²⁵.

Fig. 3 | Physical properties of the Galactic Centre chimneys. **a**, Surface brightness, density and pressure latitudinal profiles of the Galactic Centre chimneys. Black and red symbols refer to fits to the data (at $l = 0^\circ$) for the northern and southern chimneys, respectively. Stars and squares show results from XMM-Newton and Chandra, respectively. To estimate densities and pressure, we assumed that the ± 15 -pc Sgr A lobes have depths of 15 pc, while all other regions have depths of 150 pc. Vertical error bars represent 1σ uncertainties; horizontal error bars show the radial range of the extraction regions. Similar characteristics are found for the northern and southern chimneys. For comparison, grey stars show the latitudinal profile at $l = -0.7^\circ$, which has a density a factor of 2–3 smaller than the chimneys ($l = 0^\circ$) at similar latitudes. Since a possible impact of varying photoelectric absorption is corrected for by spectral fitting, this plot shows that the chimneys are indeed denser than the surrounding regions. The grey dotted and dashed lines show the density stratification for a static or non-rotating and isothermal atmosphere embedded in the gravitational potential of the Milky Way with temperature of $kT = 0.6$ keV and 1 keV, respectively. For illustration, the curves are normalized in order to reproduce the densities observed at $l = -0.7^\circ$. In the inner region corresponding to ± 15 -pc bipolar lobes, the density gradient is clearly much steeper than expected for the hydrostatic atmosphere. For larger radii, a drop in density of a factor of about 2 could be attributed to the Milky Way gravitational potential. **b**, Temperature-versus-density plot for the latitudinal profiles at $l = 0^\circ$. Two groups of points correspond to the ± 15 -pc bipolar lobes and the chimneys, respectively. Although each group might be consistent with the adiabatic (iso-entropic) law for the gas with the adiabatic index $\gamma = 5/3$, the normalizations are very different. This shows that the chimneys are not a simple adiabatic continuation of the outflow of the ± 15 -pc lobes.

In the direction perpendicular to the Galactic plane, the chimneys extend beyond one degree, where they appear to merge with the Fermi bubbles, as suggested by the extrapolation of the boundaries of the extended structures seen in ROSAT images⁶ to small latitudes (Extended Data Figs. 1, 4). We tentatively associate the transition from the chimneys to the Fermi bubbles with a modest drop of temperature, which in the northern chimney occurs about 160 pc above the plane. In the surface brightness distribution, the transition is also relatively inconspicuous.

With these new data, two questions arise. One is whether the inner ± 15 -pc bipolar lobes and the larger 160-pc chimneys are parts of the same outflow that starts very close to Sgr A*. While this cannot be entirely excluded owing to the likely intermittency of the energy injection from the central regions, the X-ray data do not directly support the idea that the chimneys are a continuation of the inner lobes. For instance, the density–temperature relations shown in Fig. 3 indicate that the entropies associated with these two flows are markedly different, as shown by the data following two separate normalizations for the adiabatic relations ($kT \propto n^{2/3}$). Indeed, the inner lobes appear to be embedded into the volume occupied by the larger chimneys, so the inner lobes could represent the most recent episode of energy injection into the chimneys, in this case from within the central parsec. One plausible candidate for such a universal mechanism is the energy released by supernovae. In this framework, it is the strongly uneven distribution of massive stars over the Galactic Centre region (one concentration close to Sgr A* and another one distributed over ± 50 pc) that leads to the nested appearance of two outflows, rather than to a single one.

Our hypothesis is that the chimneys could be the channel that transports the energy from the active Galactic Centre region to the Fermi bubbles, as their morphology suggests. The various estimates of the power needed to create and sustain the Fermi bubbles differ by several orders of magnitude, from a few 10^{40} erg s^{-1} to 10^{44} erg s^{-1} , depending on the assumed source of energy and its intermittency^{4,26,27}. The lower end of these estimates is within an order of magnitude of the chimney energetic, which is plausibly a lower limit, since only a fraction of the energy flowing through this channel might be deposited into the X-ray-emitting gas. The ‘low-power’ models of the Fermi bubbles are predominantly associated with quasi-continuous star-formation wind settings^{26,28} and the observed morphology of the chimney is

reminiscent of these wind models, albeit with some modifications, for example, related to the shape of the ‘nozzle’ that confines the flow over approximately 100 pc. In the supernovae-powered framework described above, the role of Sgr A* (and the ± 15 -pc bipolar lobes) is subdominant, assuming that the distribution of massive stars is a good proxy for the spatial distribution of the energy release. However, extremely energetic events associated with accretion episodes onto Sgr A*, such as tidal disruption events and episodic instances of active-galactic-nucleus-like accretion activity, remain a viable framework too^{29,30}. In this case, the channel manifested as the chimneys could facilitate the propagation of matter and energy from Sgr A* to the rarefied and low-pressure regions above the disk (see ref.²⁸).

Online content

Any methods, additional references, Nature Research reporting summaries, source data, statements of data availability and associated accession codes are available at <https://doi.org/10.1038/s41586-019-1009-6>.

Received: 6 November 2018; Accepted: 30 January 2019;

Published online 20 March 2019.

- Ponti, G., Morris, M. R., Terrier, R. & Goldwurm, A. in *Cosmic Rays in Star-Forming Environments* (eds Torres, D. & Reimer, O.) 331–369 (Astrophysics and Space Science Proceedings Vol. 34, Springer, Berlin, 2013).
- Morris, M. et al. Deep X-ray imaging of the central 20 parsecs of the Galaxy with Chandra. *Astron. Notes Suppl.* **324**, 167–172 (2003).
- Zhao, J.-H., Morris, M. R. & Goss, W. M. A new perspective of the radio bright zone at the Galactic Center: feedback from nuclear activities. *Astrophys. J.* **817**, 171–187 (2016).
- Su, M., Slatyer, T. R. & Finkbeiner, D. P. Giant gamma-ray bubbles from Fermi-LAT: active galactic nucleus activity or bipolar galactic wind? *Astrophys. J.* **724**, 1044–1082 (2010).
- Snowden, S. L. et al. ROSAT Survey diffuse X-ray background maps. II. *Astrophys. J.* **485**, 125–135 (1997).
- Bland-Hawthorn, J. & Cohen, M. The large-scale bipolar wind in the Galactic Center. *Astrophys. J.* **582**, 246–256 (2003).
- Sofue, Y. & Handa, T. A radio lobe over the Galactic Centre. *Nature* **310**, 568–569 (1984).
- Law, C. J. A multiwavelength view of a mass outflow from the Galactic Center. *Astrophys. J.* **708**, 474–484 (2010).
- Ponti, G. et al. The XMM-Newton view of the central degrees of the Milky Way. *Mon. Not. R. Astron. Soc.* **453**, 172–213 (2015).
- Genzel, R., Eisenhauer, F. & Gillessen, S. The Galactic Centre massive black hole and nuclear star cluster. *Rev. Mod. Phys.* **82**, 3121–3195 (2010).
- Kataoka, J. et al. Suzaku observations of the diffuse X-ray emission across the Fermi bubbles’ edges. *Astrophys. J.* **779**, 57–73 (2013).
- Heard, V. & Warwick, R. S. XMM-Newton observations of the Galactic Centre Region—II. The soft-thermal emission. *Mon. Not. R. Astron. Soc.* **434**, 1339–1354 (2013).
- Chevalier, R. A. & Clegg, A. W. Wind from a starburst galaxy nucleus. *Nature* **317**, 44–45 (1985).
- Heckman, T. M., Armus, L. & Miley, G. K. On the nature and implications of starburst-driven galactic superwinds. *Astrophys. J. Suppl.* **74**, 833–868 (1990).
- Suchkov, A. A., Balsara, D. S., Heckman, T. M. & Leitherer, C. Dynamics and X-ray emission of a galactic superwind interacting with disk and halo gas. *Astrophys. J.* **430**, 511–532 (1994).
- Krumholz, M. R., Kruijssen, J. M. D. & Crocker, R. M. A dynamical model for gas flows, star formation and nuclear winds in galactic centres. *Mon. Not. R. Astron. Soc.* **466**, 1213–1233 (2017).
- Rees, M. J. Tidal disruption of stars by black holes of 10^6 to 10^8 solar masses in nearby galaxies. *Nature* **333**, 523–528 (1988).
- Generozov, A., Stone, N. C. & Metzger, B. D. Circumnuclear media of quiescent supermassive black holes. *Mon. Not. R. Astron. Soc.* **453**, 775–796 (2015).
- Lu, J. R. et al. Stellar populations in the central 0.5 pc of the Galaxy. II. The initial mass function. *Astrophys. J.* **764**, 155–172 (2013).
- Morris, M. The Galactic Center magnetosphere. *J. Phys. Conf. Ser.* **54**, 1–9 (2006).
- Crocker, R. M., Jones, D. I., Melia, F., Ott, J. & Protheroe, R. J. A lower limit of 50 microgauss for the magnetic field near the Galactic Centre. *Nature* **463**, 65–67 (2010).
- Eatough, R. P. et al. A strong magnetic field around the supermassive black hole at the centre of the Galaxy. *Nature* **501**, 391–394 (2013).
- Mauerhan, J. C., Muno, M. P., Morris, M. R., Stolovy, S. R. & Cotera, A. Near-infrared counterparts to Chandra X-ray sources toward the Galactic Center. II. Discovery of Wolf-Rayet stars and O supergiants. *Astrophys. J.* **710**, 706–728 (2010).
- Dong, H., Wang, Q. D. & Morris, M. R. A multiwavelength study of evolved massive stars in the Galactic Centre. *Mon. Not. R. Astron. Soc.* **425**, 884–906 (2012).
- Strickland, D. K. & Stevens, I. R. Starburst-driven galactic winds—I. Energetics and intrinsic X-ray emission. *Mon. Not. R. Astron. Soc.* **314**, 511–545 (2000).
- Crocker, R. M. & Aharonian, F. Fermi bubbles: giant, multibillion-year-old reservoirs of Galactic Center cosmic rays. *Phys. Rev. Lett.* **106**, 101102 (2011).
- Kataoka, J. et al. X-ray and gamma-ray observations of the Fermi bubbles and NPS/loop I structures. *Galaxies* **6**, 27 (2018).
- Lacki, B. C. The Fermi bubbles as starburst wind termination shocks. *Mon. Not. R. Astron. Soc.* **444**, L39–L43 (2014).
- Bland-Hawthorn, J., Maloney, P. R., Sutherland, R. S. & Madsen, G. J. Fossil imprint of a powerful flare at the Galactic Center along the Magellanic stream. *Astrophys. J.* **778**, 58–74 (2013).
- Roberts, S. R., Jiang, Y.-F., Wang, Q. D. & Ostriker, J. P. Towards self-consistent modelling of the Sgr A* accretion flow: linking theory and observation. *Mon. Not. R. Astron. Soc.* **466**, 1477–1490 (2017).

Acknowledgements This work is dedicated to the memory of A. M. Ponti, who contributed to its realization by focusing the energy and motivation of G.P. G.P. thanks A. Merloni for discussions and the Max-Planck-Institut für Astronomie Heidelberg for hospitality. This research has made use of data obtained both with XMM-Newton, an ESA science mission with instruments and contributions directly funded by ESA Member States and NASA, and with the Chandra Data Archive and software provided by the Chandra X-ray Center. G.P. and F. Hofmann acknowledge financial support from the Bundesministerium für Wirtschaft und Technologie/Deutsches Zentrum für Luft- und Raumfahrt (BMW/DLR; grants FKZ 50 OR 1604, FKZ 50 OR 1715 and FKZ 50 OR 1812) and the Max Planck Society. A.G. and R.T. acknowledge support from CNES and ANR (grant ANR-17-CE31-0014) and M.R.M. acknowledges support from NASA.

Reviewer information Nature thanks Masha Chernyakova and the other anonymous reviewer(s) for their contribution to the peer review of this work.

Author contributions G.P. and M.R.M. conceived and successfully proposed the two XMM-Newton large projects that led to this work. F. Haberl ran and improved the advanced mosaicking pipeline for XMM-Newton data developed by the high-energy group at MPE. F. Hofmann performed the mosaicking of the Chandra data, and implemented the contour-binned spectral extraction technique and advanced smoothing techniques. G.P. and F. Hofmann performed the spectral analysis. E.C. verified all analysis tasks employing an alternative pipeline. G.P., F. Hofmann, E.C. and M.R.M. led the interpretation, modelling and discussion of this work and together they wrote the manuscript. F. Haberl, K.N., R.T., M.C. and A.G. read and commented on the manuscript.

Competing interests The authors declare no competing interests.

Additional information

Extended data is available for this paper at <https://doi.org/10.1038/s41586-019-1009-6>.

Reprints and permissions information is available at <http://www.nature.com/reprints>.

Correspondence and requests for materials should be addressed to G.P.

Publisher’s note: Springer Nature remains neutral with regard to jurisdictional claims in published maps and institutional affiliations.

© The Author(s), under exclusive licence to Springer Nature Limited 2019

METHODS

Data reduction and analysis. Our results are based on smoothed X-ray images in different energy bands and spectra of the diffuse X-ray emission of the innermost Galactic corona³¹. We refer here to the Galactic corona, as initially named by^{32,33} as the hot X-ray-emitting plasma composing the hot interstellar medium phase and connecting it to the Galactic halo^{34,35}. The X-ray maps are based on two recent XMM-Newton large observing programmes comprising 46 observations of 25-ks exposure (see Extended Data Fig. 2), in addition to all the available archival data (mainly concentrating on the scan of the central molecular zone⁹). All new observations are performed with the European Photon Imaging Camera (EPIC) PN³⁶ and MOS charge-coupled devices (CCDs)³⁷, in full-frame CCD readout mode with the medium optical filters applied. The XMM-Newton data reduction was performed using the Science Analysis System version 16.1.0 (<https://www.cosmos.esa.int/web/xmm-newton/what-is-sas>). For more details on the analysis pipeline see refs^{9,38}. Data products were downloaded from the respective archives. We screened times of high background and removed point sources. Detector background files were created and subtracted using the task ‘evqpb’, summing filter-wheel-closed files to have ten times the exposure of each observation.

We also used archival observations with the Chandra Advanced CCD Imaging Spectrometer³⁹ imaging (ACIS-I) CCD array (energy range of about 0.1 keV to 10 keV). The Chandra ACIS-I observations were reprocessed using the Chandra Interactive Analysis of Observations software package⁴⁰ version 4.5 and the Chandra Calibration Database version 4.5.9. For a detailed description of the data reduction pipeline see ref.⁴¹. We estimated the background in each Chandra observation via the CIAO tool ‘acis_bkgrnd_lookup’, which delivers a suitable blank-sky background file, provided by the Chandra X-ray centre⁴². The Chandra data have an exposure of about 50 ks in the central scan, 15 ks in the latitudinal extensions, and 2 ks in the large areas at higher latitude (see Extended Data Fig. 4).

The combination of Chandra and XMM-Newton data provides the highest spatial (about 1 arcsec) and spectral resolution (about 100 eV full-width at half-maximum, FWHM) available in soft X-rays.

For the XMM-Newton data we performed source detection on each individual observation and all detected point sources have been masked out. Readout streaks were included in background images. For Chandra data, we performed source detection on all datasets, simultaneously in multiple energy bands. A second point-source detection was run on the merged images and, after carefully screening the detection list, the point sources were masked out from the image (in some cases additional regions were masked to screen dust-scattering halos and readout streaks of very bright sources). We then computed the background-subtracted, exposure-corrected and adaptively smoothed images, resulting in smoothed flux images of diffuse emission (foreground, unresolved point sources, and intrinsic hot plasma emission from the Galactic Centre).

The flux images were then binned into regions of equal signal-to-noise (S/N) ratio 50 ($>2.5 \times 10^3$ counts per bin) for Chandra and S/N 100 ($>1 \times 10^4$ counts per bin) for XMM-Newton. We estimated the minimum number of counts per bin by assuming zero background. We used the definition of $S/N = \text{counts}/\sqrt{\text{counts}}$ in the case without background. This is why $(S/N)^2$ is the minimum number of counts per bin. For a detailed description of the binning technique ‘contbin’ applied here see ref.⁴³. The difference was chosen because Chandra has a more stable background than does XMM-Newton. The contour binning technique ‘contbin’⁴³ was used for this task. For each observation overlapping with one of the bins, spectra and response files were created and all contributions were added with proper weighting to obtain one spectrum for each spatial bin. These small-scale bins were then added up to obtain higher S/N spectra for regions of interest (see Extended Data Figs. 5 and 6). Each of the regions shown in Extended Data Figs. 5 and 6 consists of 5–7 merged initial bins. The spectra in the 0.5–7-keV energy range were then fitted with emission models using XSPEC⁴⁴ version 12.9.1n. The best-fit parameters were used to derive the profiles shown in Figs. 2, 3 and Extended Data Fig. 7.

We identified the following XSPEC model as the best general description of the data (unless stated otherwise for tests): TBABS (APEC + POW + GAUSS + GAUSS) + TBABS APEC, where the first foreground absorption (TBABS model) is the absorption towards the Galactic Centre, the first APEC model is the intrinsic ~ 1 -keV plasma at the Galactic Centre, the POW and the two GAUSS models describe the power law and two narrow Gaussian lines at 6.4 keV and 6.7 keV caused by unresolved point sources around the Galactic Centre and non-thermal emission¹ (the photon index of the power law was fixed to $\Gamma = 1.8$). The second APEC model with lower foreground absorption (0.7×10^{22} cm⁻²) and a temperature of about 0.2 keV describes a ‘foreground’ emission (that is, between the observer and the Galactic Centre, for example, such as the contribution from the local bubble) that was observationally chosen to fit the data. Throughout this work we used the APEC model for collisionally ionized diffuse gas, which is based on the ATOMDB code, version 3.0.7⁴⁵. Uncertainties are quoted at the 1σ level unless stated otherwise. Abundances are described according to the solar

abundances from ref.⁴⁶. The distance to the Galactic Centre was assumed to be 8 kpc (ref.⁴⁷).

The profiles shown in Figs. 2, 3 and Extended Data Fig. 7 are derived from the best-fit values of the APEC model to the intrinsic ~ 1 -keV plasma component at the Galactic Centre. The free fit parameters are the plasma temperature T (in kiloelectronvolts) and the model normalization η (in units of cm⁻⁵). We define surface brightness as the normalization of the best-fit APEC model divided by the extraction area in arcminutes squared (see ref.⁴¹ for more details). Density n (in units of cm⁻³) and pressure P (in units of keV cm⁻³) were derived assuming full ionization with 10% helium and 90% hydrogen (that is, $n_e \approx 1.2n_p$). For a definition of η and a detailed description of the APEC model, see the XSPEC manual: <https://heasarc.gsfc.nasa.gov/xanadu/xspec/XspecManual.pdf>.

$$n = \sqrt{\eta \times \frac{19.3\pi D_A^2}{V}} \quad (1)$$

$$P = T \times n \quad (2)$$

where D_A is the distance to the source in centimetres and V is the assumed volume in cubic centimetres. The volume was calculated as the extraction surface area multiplied by the assumed depth. For the ± 15 -pc bipolar lobes we assumed a constant depth of 15 pc. For the remaining diffuse emission, we assumed a uniform depth of 150 pc, as suggested by the width of the chimneys. A caveat of this approach is that the density beyond the chimneys, at the foot of the Fermi bubbles, might be overestimated by a large factor, because that emission probably comes from a much larger volume. Indeed, if we assume a depth of 1.5 kpc for the high-latitude emission, the expected particle density would drop to about 10^{-2} cm⁻³.

Comparing the surface brightness of the X-ray counterparts of the Fermi bubbles in ROSAT images with the high-latitude emission observed with XMM-Newton, we found good agreement. The photon count rate in a ROSAT 1–2-keV (assuming an effective area of about 60 cm²) mosaic image (Extended Data Fig. 1) and between 1 keV and 2 keV in the XMM-Newton image (about 1,500 cm²) of the same band are consistent at about 3×10^{-6} s⁻¹ cm⁻² arcmin⁻².

Morphology of the northern chimney and its connection with the Galactic Centre lobe. As shown in Fig. 1 and Extended Data Fig. 2, the northern chimney shows a complex morphology. Indeed, the emissivity peak does not appear at the centre of the chimney, as would be expected in case of emission from plasma filling a cavity. Instead, increased emission appears to trace the edges of the northern chimney (Fig. 1, Extended Data Figs. 2 and 7). By performing spatially resolved spectral analysis, we verified that the lower emissivity at the centre of the northern chimney is not an artefact of enhanced X-ray obscuration.

By performing a continuum-subtracted S xv map (Extended Data Fig. 3), we also noted that the western edge of the northern chimney (at $l \approx -0.5$ – 0.6°) appears rather sharp on a scale of roughly a hundred parsecs. This corresponds well to the location of AFGL5376, the most prominent portion of a strong, large-scale (about 90 pc) shock front⁴⁸. The edge in the plasma distribution does not correspond to the western edge of the Galactic Centre lobe (Extended Data Fig. 2); instead it corresponds to the transition from non-thermal to thermal radio emission⁴⁹. Further out, at the position of the thermal western part of the Galactic Centre lobe, there are shocks, molecular clouds moving at high speed and radio filaments^{6,48}. It is possible that this is the region where the outflow impacts ambient clouds in the interstellar medium.

We performed detailed spectral fitting and we compared the emission inside the chimneys ($l = 0^\circ$) with the dark region outside its western edge (at $l \approx -0.7^\circ$). This comparison verified that the emissivity drop observed at the western edge of the northern chimney corresponds to a real variation in the properties of its hot plasma and is not simply due to increased obscuration induced by the presence of such interstellar medium clouds (see Figs. 2, 3 and Extended Data Figs. 5–7).

Extended Data Figure 3 shows that the western edge of the northern chimney continues in a remarkably straight line along the western edge of the southern chimney. This appears to reinforce the idea that the chimneys are two manifestations of the same physical process.

Other sources powering the bipolar lobes of Sgr A. In the main text we suggested that Sgr A’s bipolar lobes are primarily powered by supernovae explosions and tidal disruption events. However, this does not exclude other processes that might contribute to powering such features.

For example, whether the current activity of Sgr A* can inflate the ± 15 -pc bipolar lobes is unclear³⁰. Studies of clusters of galaxies demonstrate that supermassive black holes accreting at low Eddington rates do generate outflows that inflate bubbles into the intracluster medium and have kinetic luminosities orders of magnitude larger than the instantaneous radiative power of these black holes^{50,51}. For Sgr A*, the quiescent radiative luminosity^{52,53} of about 10^{36} erg s⁻¹, when expressed in Eddington units, is far lower than for the black holes in galaxy clusters, firmly placing this object deep into a very low-luminosity regime⁵⁴. It is plausible

that in this regime the outflow power could exceed the radiative luminosity by a large factor, opening up the possibility that Sgr A* could provide the mechanical luminosity needed to power the ± 15 -pc Sgr A bipolar lobes, even without invoking additional tidal-disruption-like major outbursts.

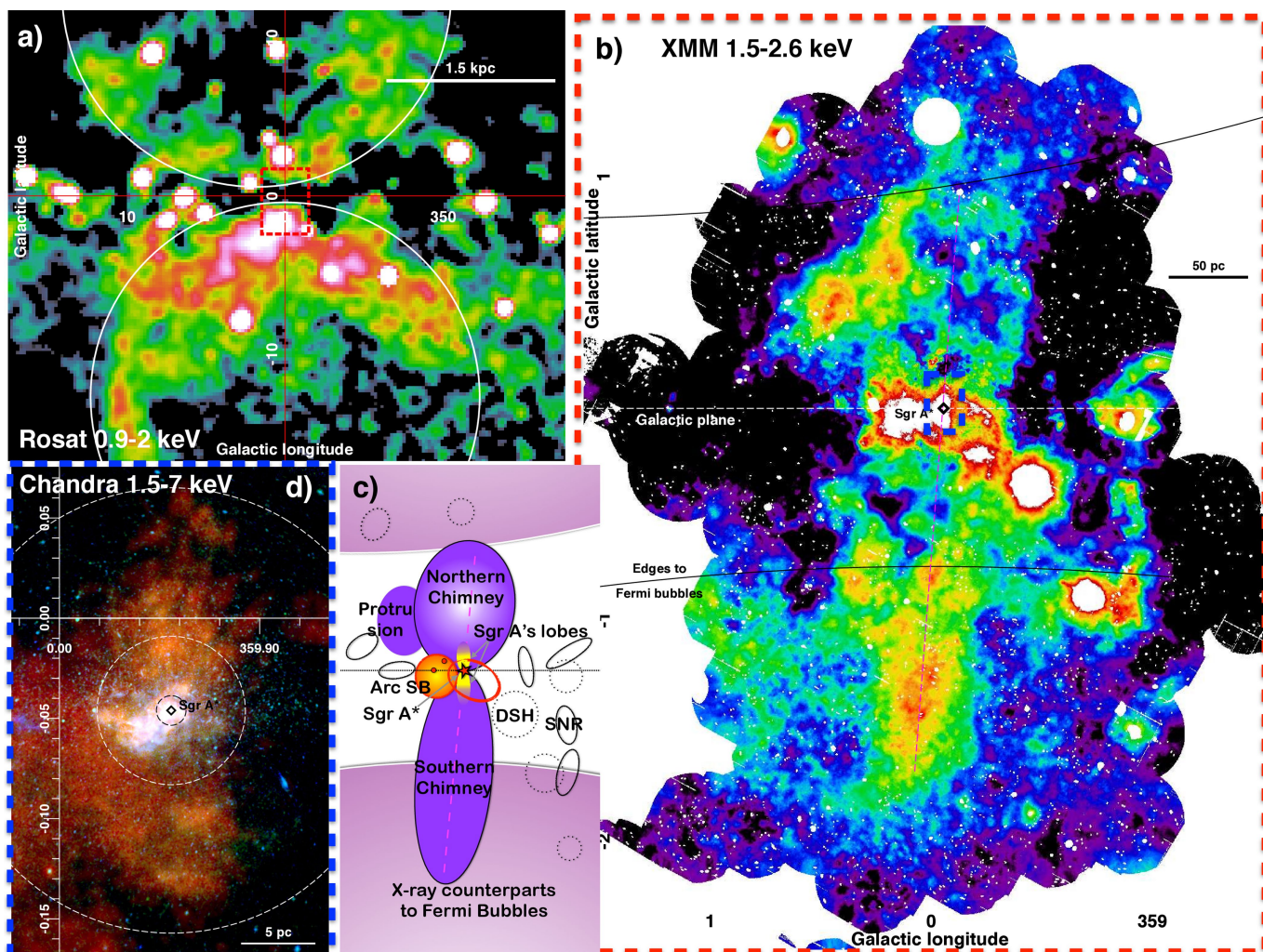
Uncertainty related to the unknown filling factor and abundances. The X-ray morphologies of all structures seen in ROSAT, XMM-Newton and Chandra images are very complex with signs of edge-brightening. It is plausible that the X-ray-emitting gas is not volume-filling, but represents patches of denser gas interacting with an outflow, as suggested by many simulations that involve rapid expansion and adiabatic cooling of matter in the outflow¹³. We nevertheless assume in the main paper the volume-filling factor $f = 1$, to derive the gas density in the observed structures and estimate their total energy content. For $f < 1$, the recovered density scales as $n_{\text{obs}} \propto n_{\text{true}} f^{1/2}$. Assuming that the energy density is uniform over the structure (in the longitudinal direction), the estimated total energy will be also lower than the true one by a factor of $f^{1/2}$ and therefore should be treated as a lower limit.

Throughout the paper, we assume solar abundances of the X-ray-emitting plasma. This assumption is adopted in order to avoid spurious degeneracies between the fitted parameters. We note that the X-ray-emitting plasma in the plane, within the central molecular zone, has solar or slightly super-solar metallicities^{9,12,55}. The metallicity is expected to drop with latitude. Indeed, the halo metallicity might be substantially lower than solar, with metallicities of the X-ray-emitting plasma of the order of about $0.3 \times$ the solar value, inside the Fermi bubbles^{11,27}. To quantify the consequences of this assumption, we fitted one of the XMM-Newton spectra of the northern chimney, changing the assumed metallicity from $1.5 \times$ to $0.3 \times$ the solar value. We observed that the best-fit temperature and emissivity changed by about 5% and about 10%, respectively.

Data and code availability

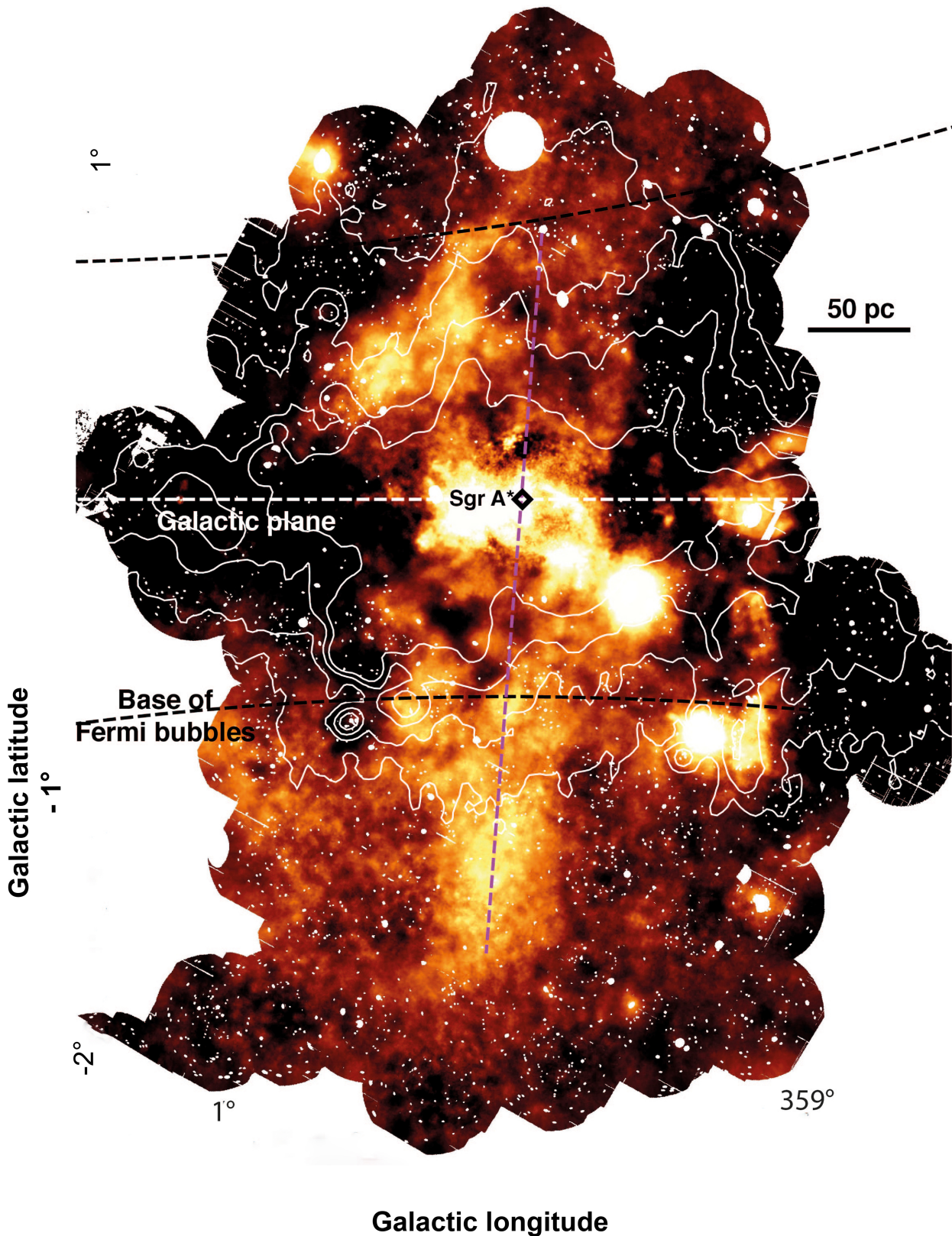
The datasets analysed during the current study and the software to perform the analysis are available in the XMM-Newton, Chandra and ROSAT repository: <http://nxa.esac.esa.int>, <https://www.cosmos.esa.int>, <http://cxc.harvard.edu> and <http://www.xray.mpe.mpg.de/rosat/archive>.

31. Spitzer, L. Jr Theories of the hot interstellar gas. *Annu. Rev. Astron. Astrophys.* **28**, 71–101 (1990).
32. Jenkins, E. B. Coronal gas in the Galaxy. I—A new survey of interstellar O vi. *Astrophys. J.* **219**, 845–860 (1978).
33. Savage, B. D. & de Boer, K. S. Observational evidence for a hot gaseous Galactic corona. *Astrophys. J.* **230**, L77–L82 (1979).
34. Ferrière, K. M. The interstellar environment of our galaxy. *Rev. Mod. Phys.* **73**, 1031–1066 (2001).
35. Cox, D. P. The three-phase interstellar medium revisited. *Annu. Rev. Astron. Astrophys.* **43**, 337–385 (2005).
36. Strüder, L. et al. The European Photon Imaging Camera on XMM-Newton: the pn-CCD camera. *Astron. Astrophys.* **365**, L18–L26 (2001).
37. Turner, M. J. L. et al. The European Photon Imaging Camera on XMM-Newton: the MOS cameras. *Astron. Astrophys.* **365**, L27–L35 (2001).
38. Haberl, F. et al. The XMM-Newton survey of the Small Magellanic Cloud. *Astron. Astrophys.* **545**, A128 (2012).
39. Garmire, G. P., Bautz, M. W., Ford, P. G., Nousek, J. A. & Ricker, G. R. Jr. Advanced CCD imaging spectrometer (ACIS) instrument on the Chandra X-ray Observatory. *Proc. SPIE* **4851**, 28–44 (2003).
40. Fruscione, A. et al. CIAO: Chandra's data analysis system. *Proc. SPIE* **6270**, 62701V (2006).
41. Hofmann, F., Sanders, J. S., Nandra, K., Clerc, N. & Gaspari, M. Thermodynamic perturbations in the X-ray halo of 33 clusters of galaxies observed with Chandra ACIS. *Astron. Astrophys.* **585**, A130 (2016).
42. Markevitch, M. et al. Chandra spectra of the soft X-ray diffuse background. *Astrophys. J.* **583**, 70–84 (2003).
43. Sanders, J. S. Contour binning: a new technique for spatially resolved X-ray spectroscopy applied to Cassiopeia A. *Mon. Not. R. Astron. Soc.* **371**, 829–842 (2006).
44. Arnaud, K. A. XSPEC: The first ten years. In *Astronomical Data Analysis Software and Systems V* Vol. 101, 17 (Astronomical Society of the Pacific Conference Series, 1996).
45. Foster, A. R., Ji, L., Smith, R. K. & Brickhouse, N. S. Updated atomic data and calculations for X-ray spectroscopy. *Astrophys. J.* **756**, 128–139 (2012).
46. Anders, E. & Grevesse, N. Abundances of the elements—meteoritic and solar. *Geochim. Cosmochim. Acta* **53**, 197–214 (1989).
47. Eisenhauer, F. et al. A geometric determination of the distance to the Galactic Center. *Astrophys. J.* **597**, L121–L124 (2003).
48. Uchida, K. I., Morris, M. R., Serabyn, E. & Bally, J. AFGL 5376: a strong, large-scale shock near the Galactic Center. *Astrophys. J.* **421**, 505–516 (1994).
49. Blanton, M. C. The Galactic Center lobe: new 14 GHz GBT observations. PhD thesis, Univ. North Carolina at Chapel Hill (2008).
50. Churazov, E., Forman, W., Jones, C. & Böhringer, H. Asymmetric, arc minute scale structures around NGC 1275. *Astron. Astrophys.* **356**, 788–794 (2000).
51. Fabian, A. C. Observational evidence of active galactic nuclei feedback. *Annu. Rev. Astron. Astrophys.* **50**, 455–489 (2012).
52. Baganoff, F. K. et al. Chandra X-ray spectroscopic imaging of Sagittarius A* and the central parsec of the Galaxy. *Astrophys. J.* **591**, 891–915 (2003).
53. Wang, Q. D. et al. Dissecting X-ray-emitting gas around the center of our Galaxy. *Science* **341**, 981–983 (2013).
54. Yuan, F. & Narayan, R. Hot accretion flows around black holes. *Annu. Rev. Astron. Astrophys.* **52**, 529–588 (2014).
55. Koyama, K. Diffuse X-ray sky in the Galactic center. *Publ. Astron. Soc. Jpn* **70**, R1, <https://doi.org/10.1093/pasj/psx084> (2018).
56. Sofue, Y. The Galactic Center lobe. *Publ. Astron. Soc. Jpn* **37**, 697–713 (1985).



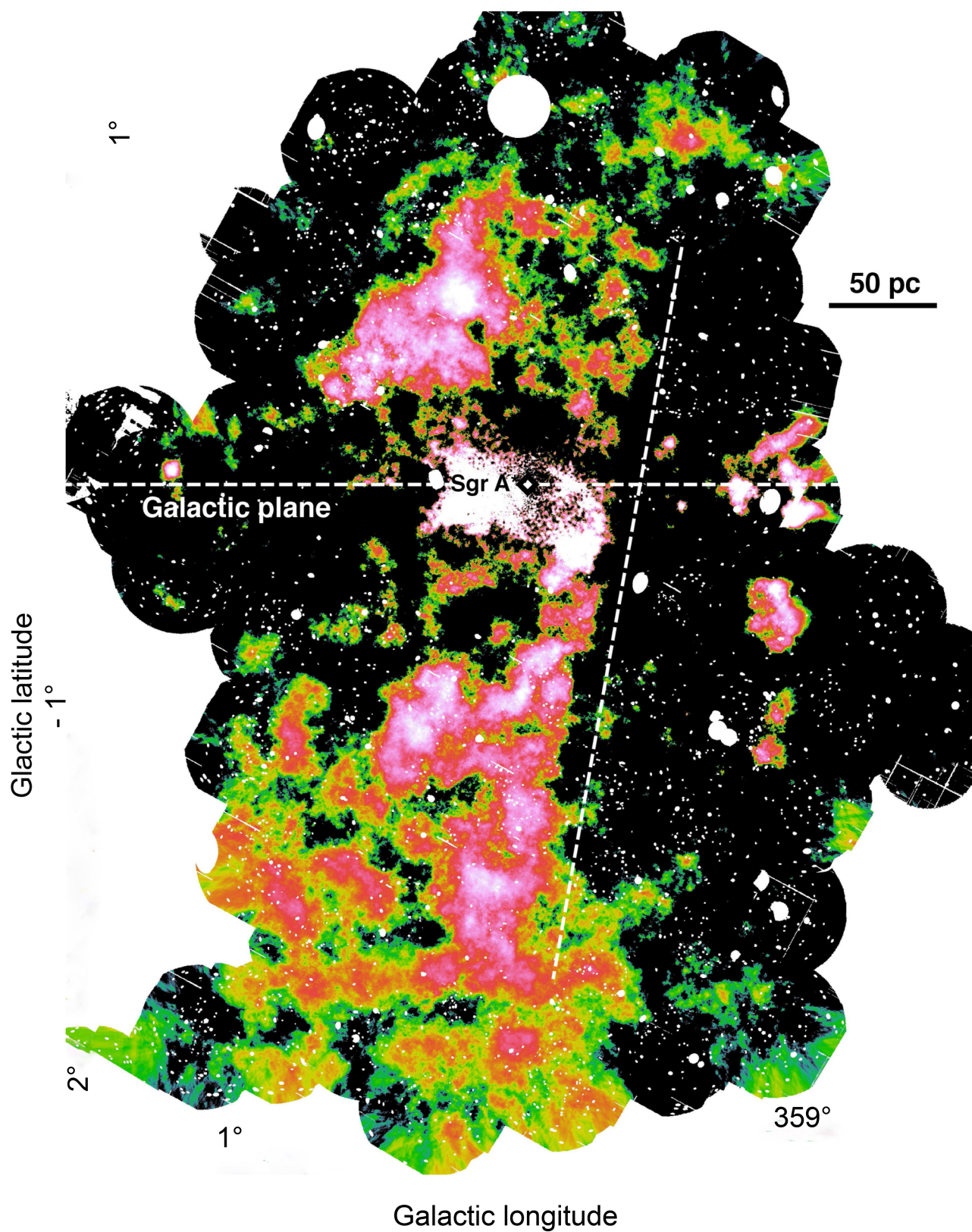
Extended Data Fig. 1 | Diffuse Galactic Centre X-ray emission at different scales. **a**, ROSAT (0.9–2-keV energy band) large-scale map of the Galactic Centre. The X-ray counterparts of the Fermi bubbles are strong X-ray emitters. The edges (white ellipses) are clearly detected on scales of several degrees, whereas they become confused (because of the short exposure of 200–300 s and soft X-ray energy band) close to the plane. The red dashed line indicates the XMM-Newton area covered by our survey. **b**, XMM-Newton map zooming into the central degrees of the Milky Way. The magenta dashed line intersects both chimneys, passing through Sgr A*. The map shows the X-ray emissivity within the 1.5–2.6-keV energy band (see Extended Data Fig. 2). **c**, Schematic view of the main diffuse X-ray-emitting features within the central 500 pc or so from Sgr A*. The red star and the yellow ellipses indicate the position of Sgr A* and of

Sgr A's ± 15 -pc bipolar lobes. The large violet ellipses indicate the location and extension of the X-ray counterpart of the Galactic Centre lobe with shell-like morphology (the northern chimney), of its eastern protrusion and of its roughly symmetric southern counterpart (the southern chimney). The orange filled ellipse, the two red circles and the red ellipse indicate the location of the Arc super-bubble (SB), the Quintuplet and Arches clusters and the super-bubble candidate G359.77–0.09 (ref. ⁸). The pink regions indicate the location of the edges to the Fermi bubbles. The dotted circles and solid ellipses indicate the position of bright X-ray sources with intense dust-scattering halos (DSH) and known supernova remnants (SNR). **d**, Chandra RGB map zooming into the central tens of parsecs of the Galaxy. The ± 15 -pc lobes are clearly visible (orange). The dashed circles have radii of 1 pc, 5 pc and 15 pc.



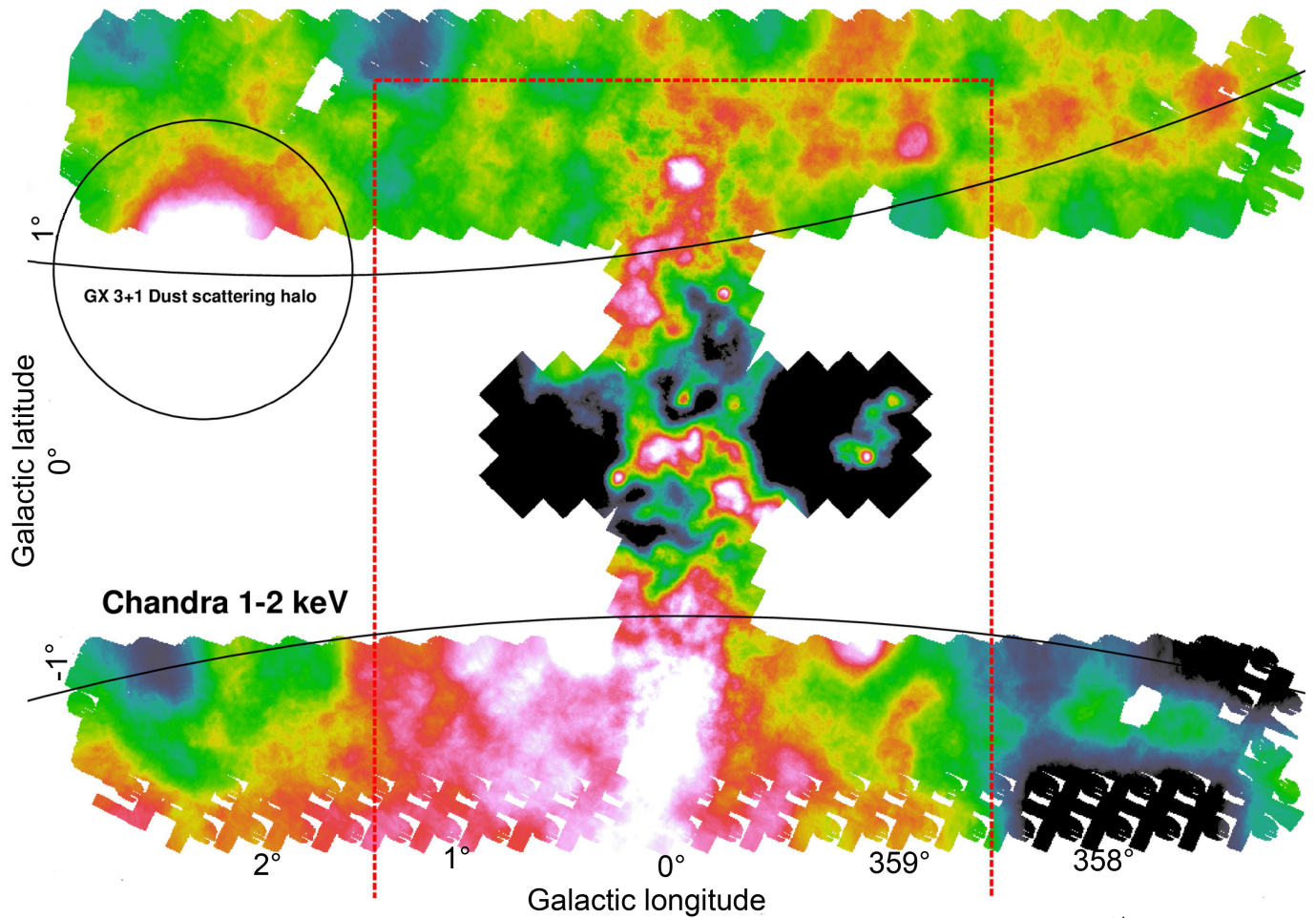
Extended Data Fig. 2 | X-ray emission from the central degrees of the Milky Way. Bright X-ray emission traces the coherent edge brightened shell-like feature, dubbed the northern chimney, located north of Sgr A* and characterized by a diameter of about 160 pc. On the opposite side, the southern chimney appears as a bright linear feature. Bright X-ray emission is observed at high latitude ($|b| \gtrsim 1^\circ$), corresponding to the X-ray counterparts of the Fermi bubble. The magenta dashed line intersects both

chimneys, passing through Sgr A*. The map shows the X-ray emissivity within the 1.5–2.6-keV energy band. The contours indicate the location of the radio Galactic Centre lobe as it appears in the background-filtered surface brightness map at 10.55 GHz (see ref. ⁵⁶). Point sources have been removed. Larger circles have been excised to remove the dust-scattering haloes around bright sources.



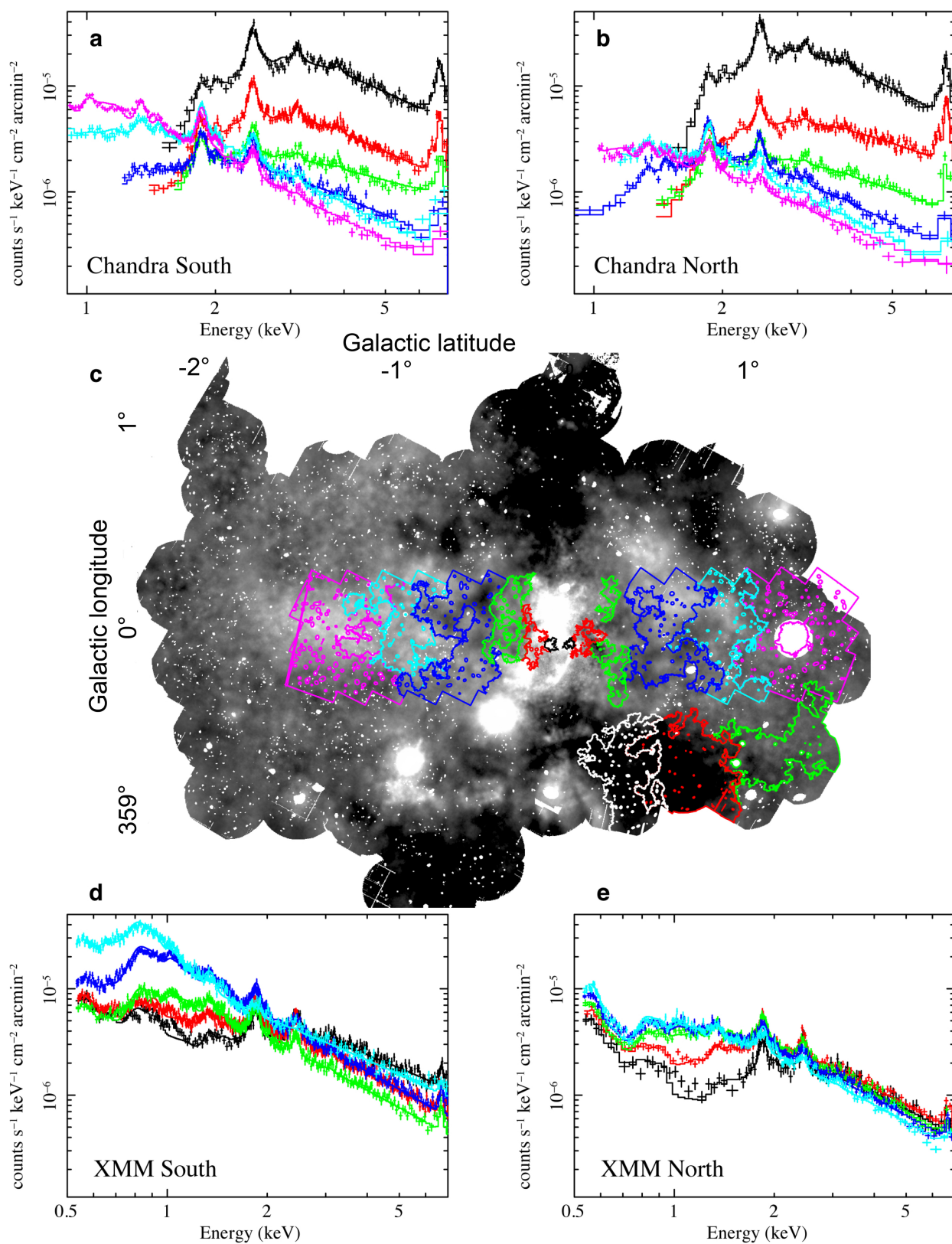
Extended Data Fig. 3 | Continuum-subtracted S xv line emission. The map highlights sources characterized by bright soft X-ray emission lines, such as diffuse thermally emitting plasma. On the other hand, point

sources and dust-scattering halos are efficiently removed. The white dashed tilted line indicates a linear ridge, about 450 pc long, that appears to run west of the chimneys.



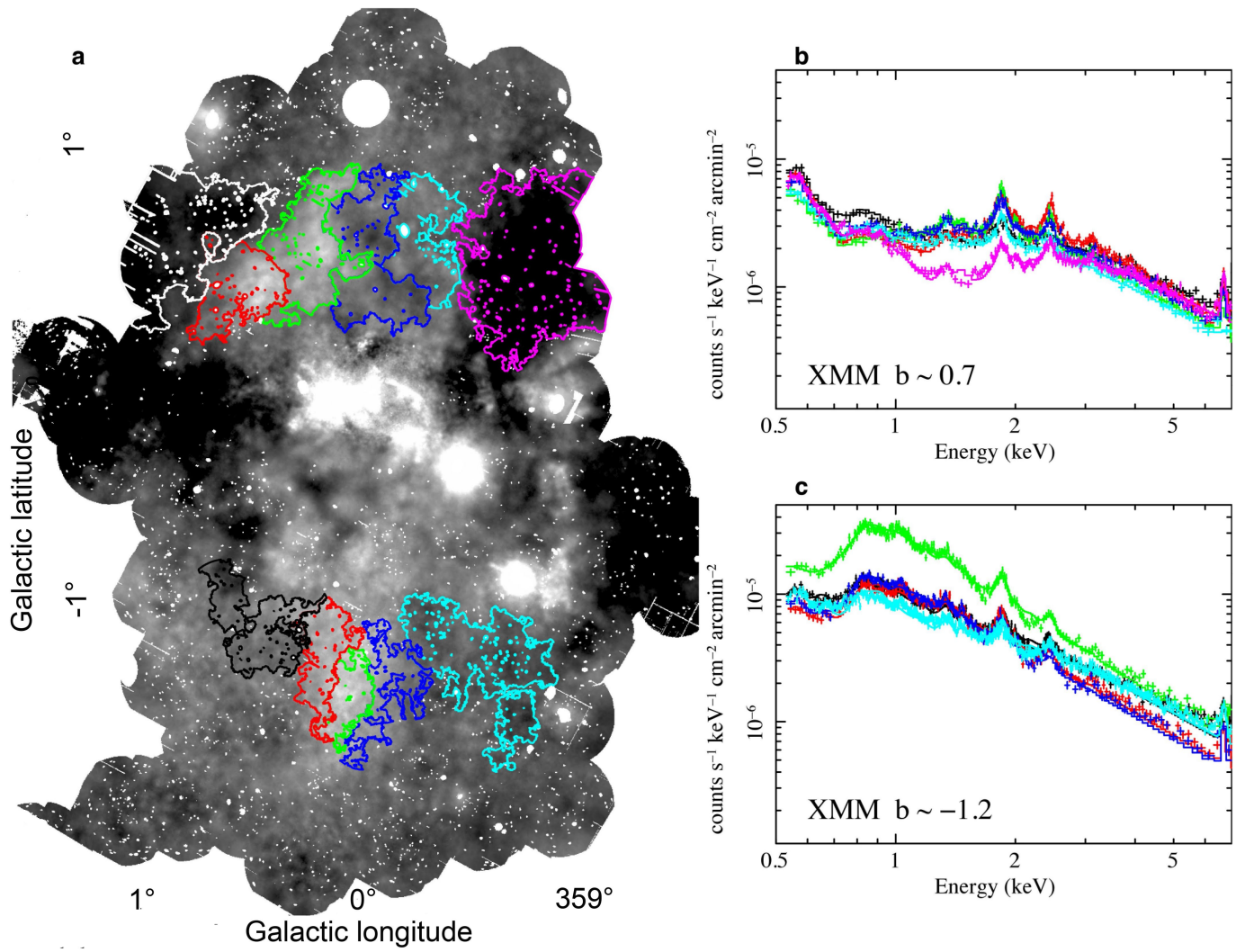
Extended Data Fig. 4 | Chandra 1–2 keV map of the Galactic Centre. The same structures seen in the XMM-Newton 1.5–2.6-keV image (Extended Data Fig. 2, footprint indicated by red dashed box) are observed also in the shallower Chandra image. Although the 1–2-keV band map

is more affected by neutral absorption towards the plane compared with the 1.5–2.6-keV band (Extended Data Fig. 2), we display it here in order to emphasize the residual high-latitude emission (for example, inside the Fermi bubbles). GX 3+1 is an accreting X-ray binary.



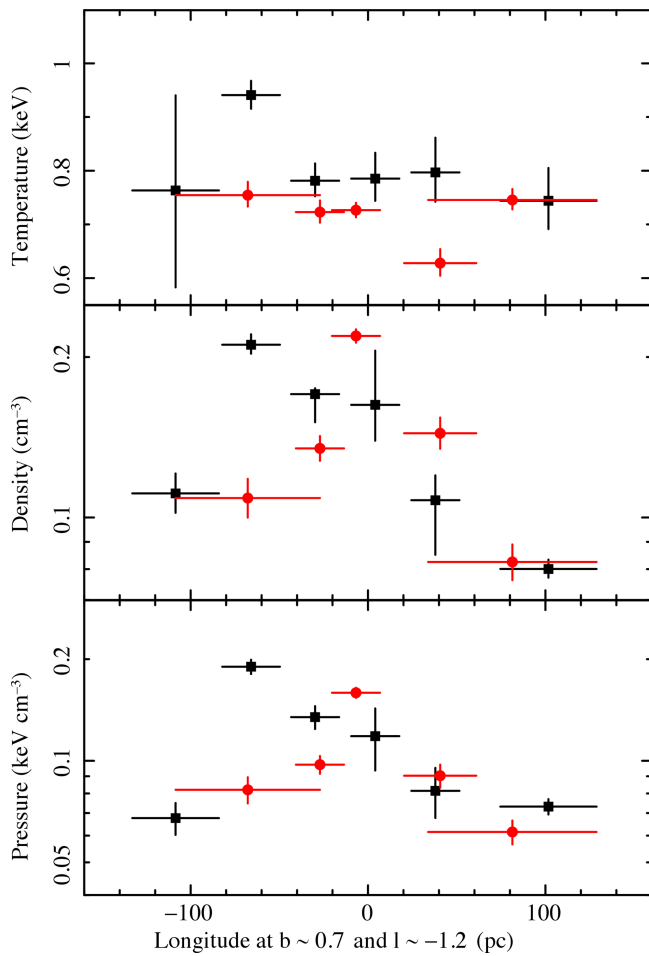
Extended Data Fig. 5 | Chandra spectra (with relative extraction regions) used to derive the physical properties of the chimneys. **a, b**, Chandra spectra used to derive the latitudinal profiles at $l = 0^\circ$ and shown in Fig. 2 for the southern (**a**) and northern (**b**) sides, respectively. **c**, XMM-Newton 1.5–2.6 keV emission map in greyscale, showing the extraction areas of the Chandra spectra used to derive the latitudinal

profiles at $l = 0^\circ$, with colours corresponding to those of the spectra. The areas at $l \approx -0.7^\circ$ indicate the extraction regions of the spectra used to derive the grey constraints in Fig. 2. **d, e**, XMM-Newton spectra used to derive the latitudinal profiles of the diffuse emission in Fig. 2. The error bars represent 1σ .



Extended Data Fig. 6 | XMM-Newton spectra (with relative extraction regions) used to derive the physical properties of the chimneys. b, c, XMM-Newton spectra used to measure the longitudinal profiles shown in Extended Data Fig. 7. a, XMM-Newton 1.5–2.6-keV map

displaying the regions used to extract the spectra corresponding to a longitudinal cut through the northern shell (at $b \approx 0.7^\circ$) and through the jet-like feature (at $b \approx -1.2^\circ$). The error bars represent 1σ .



Extended Data Fig. 7 | Longitudinal profiles of the physical properties of the chimneys. From top to bottom, temperature, density and pressure profiles are shown as a function of longitude cutting through the northern and southern chimneys at latitudes $b \approx 0.7^\circ$ and $b \approx -1.2^\circ$ (see Extended Data Fig. 6). Positive values indicate Galactic west ('west' is 'right' as in an image in Galactic coordinates b and l). Black squares and red circles indicate the longitudinal cut through the northern and southern chimneys, respectively. The densities have been estimated assuming a volume $V = (\text{PA})^{3/2}$, where PA is the projected area. Vertical error bars represent 1σ uncertainties; horizontal error bars show the radial range of the extraction regions.